Environ. Sci. Technol. **2007**, *41,* 7303−7308

Solubility of Hematite Revisited: Effects of Hydration

JE-HUN JANG,* BRIAN A. DEMPSEY, AND WILLIAM D. BURGOS

Environmental Engineering, The Pennsylvania State University, 212 Sackett Building, University Park, Pennsylvania 16802

Measured pH and dissolved ferric iron concentration ($[Fe(III)_{diss}]$) in contact with well-characterized hematite indicated an equilibrium with hematite immediately after synthesis, but $[Fe(III)_{diss}]$ increased with hydration time to be consistent with the predicted solubility of goethite or hydrous ferric oxide (HFO), hydrated analogues of hematite. X-ray diffraction did not detect structural modification of hematite after 190 days of hydration, but Mössbauer spectroscopy detected hydration that penetrated several crystalline layers. When the hematite suspension was diluted with water, solids were invariably identified as hematite, but $[Fe(III)_{diss}]$ and pH indicated an equilibrium with goethite or HFO. This is the first experimental confirmation that the interfacial hydration of anhydrous hematite results in higher solubility than predicted by bulk thermodynamic properties of hematite. Correspondence of the results with previously published measurements and implications for environmental chemistry of ferric oxides are also discussed.

Introduction

The activity of aqueous Fe^{3+} ($\{Fe^{3+}\}$) is a critical factor in assessing geochemical cycling and bioavailability of iron (*1*) and redox reactions in anoxic environments (*2*, *3*). $\{Fe^{3+}\}$ is mainly controlled by the solubility of ferric (oxyhydr)oxides. Hematite is reported to be thermodynamically the most stable of the ferric (oxyhydr)oxides and therefore the least soluble (*4*, *5*). Various compilations are in agreement about the Gibbs free energy of formation of hematite at 298.15 K ($\Delta G_f°$), reported as −743.5 (*6*), −744.4 (*7*), and −746.4 (*8*) kJ/mol.

The basic structural unit of most ferric (oxyhydr)oxides is the octahedron where Fe^{3+} is coordinated to six surrounding ligands (O^{2-}, OH^-, and/or H_2O). Different linkages among the octahedra are attributed to various phases (e.g., corner-, edge-, and/or face-shared). In hematite, Fe^{3+} is octahedrally coordinated to O^{2-}, and Fe^{3+} occupies 2/3 of the available octahedral sites for electrical neutrality (*9*). Theoretically, neither hydroxyl ions nor water molecules are present within bulk hematite.

Our experimental objective of measuring the aqueous solubility of hematite was motivated by several theoretical and experimental investigations of the hydration of hematite that analyzed possible interconversion between goethite and hematite. On the basis of individual heats of solution at 70 °C (*10*) and the heat capacity of goethite and hematite at 25 °C (ref *11*, as cited in ref *7*), Langmuir (*12*, *13*) estimated that the relative stabilities of goethite and hematite depended on the particle size at 25 °C and that coarse-grained goethite (>1 μm) was stable relative to coarse-grained hematite (>1 μm) in water at 25 °C. Tritium-exchange and discontinuous titrations of hematite indicated that the hydrated interface of hematite is goethite-like and extends 2.6−3.4 nm into the solid phase (*14*−*16*). Heat of immersion results suggested that the hydrated surface of hematite is multilayered (*17*, *18*). The reduction potentials of Fe(II)−Fe(III) measured in the presence of hematite were higher (less reducing) than predicted from its thermodynamic solubility (*19*). Measured and calculated reduction potentials were in agreement with solubility predictions for hydrous ferric oxide (HFO) (*2*, *20*). Previously, these anomalies have been attributed to poor electrochemical equilibration with the electrode (*20*). Advanced instrumental analyses have demonstrated the existence of hydrated and isolated Fe^{3+} on hematite surfaces (*21*, *22*). The water vapor pressure required to observe the conversion of a hematite (0001) surface to FeOOH or $Fe(OH)_3$ under X-ray photoemission spectroscopy (XPS) was lower than the theoretical pressure for the conversion by more than five orders of magnitude (*23*), while a previous XPS study revealed no evidence for hydration of hematite (*24*). Catalano et al. (*25*, *26*) used X-ray standing wave measurements to identify the sorption configuration of Se and As onto wet hematite and invoked that hematite surface structures different from ideal bulk termination should be considered to precisely describe the structure of adsorbed species.

Surprisingly, while these theoretical and experimental results of the hydration have been reported, simultaneous determination of dissolved ferric iron concentration ($[Fe(III)_{diss}]$), pH, and mineralogy at ambient temperature is completely lacking (*9*). Rather, the aqueous solubility of hematite at ambient temperature has been estimated based on the Gibbs free energies of formation ($\Delta G_f°$) from bulk analyses, and the estimated solubility has been applied to interpret the aqueous systems involving hematite without questioning the consequence of the interfacial hydration of hematite. The $\Delta G_f°$ value for hematite is computed from the heat of formation ($\Delta H_f°$) and the entropy of formation ($\Delta S_f°$) for hematite, which requires the measurements of heat of solution and heat capacity, respectively (*8*, *27*−*29*). The heat capacity measurements involve thermal equilibration throughout the bulk solid in the absence of water (*30*).

In this study, we sought answers for the following questions: does the hydration of hematite result in the partial conversion of the solid/water interface to more soluble phase(s) (e.g., goethite) as argued by Langmuir (*12*, *13*)? Does interfacial conversion occur without any experience of supersaturation with respect to the new phase(s)? If both questions can be answered affirmatively, then we can conclude that the interfacial hydration of hematite is spontaneous and that $\{Fe^{3+}\}$ in the presence of hematite should be higher than predicted by the thermodynamic parameters of bulk hematite.

Materials and Methods

General. All chemicals were reagent grade or better. Containers were soaked in 10% nitric acid and rinsed with deionized distilled water (DI water). All reactors were mixed at 60 rpm throughout the experiments. The 1,10-phenanthroline (*31*) or ferrozine method (*32*) was used for $[Fe(III)_{diss}]$ after reducing Fe(III) with hydroxylamine hydrochloride (*31*). The calibration range was from 1 to 20 ppm, and the accuracy and precision were better than 2%. The pH was measured using a sleeve-junction glass combination electrode; calibration standards included 0.1 and 0.01 M HCl to compensate

* Corresponding author phone: (814)865-1226; fax: (814)863-7304; e-mail: jhjang2004@gmail.com.

10.1021/es070535t CCC: $37.00
Published on Web 09/29/2007

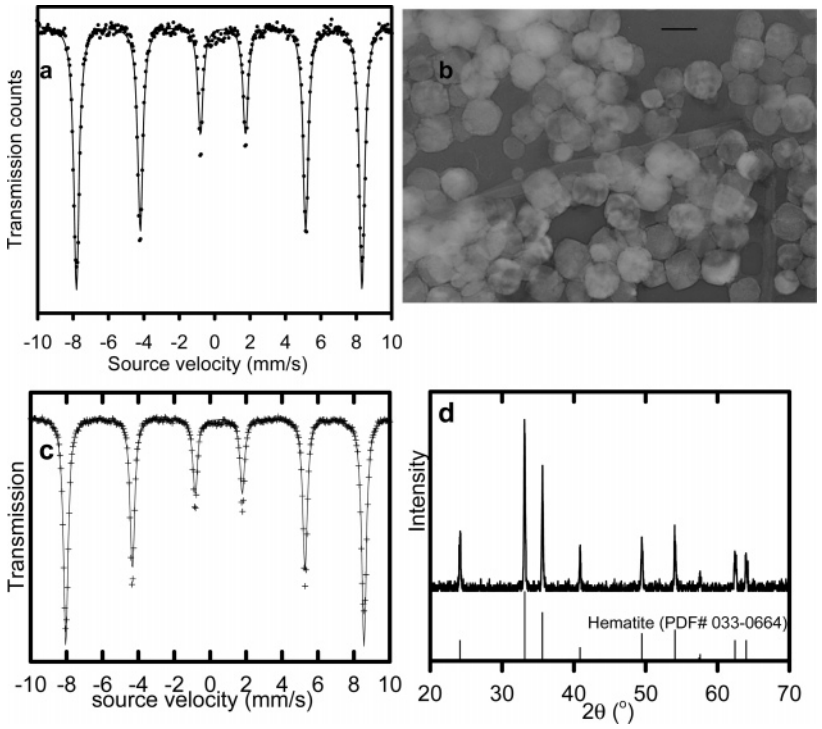

FIGURE 1. (a) MBS and (b) TEM of synthetic hematite collected on day 1 at room temperature. Scale bar in panel b is 100 nm. (c) MBS and (d) XRD pattern of commercial hematite. Peaks of reference hematite were also illustrated for comparison in panel d (Powder Diffraction File number (PDF#) 033-0664).

for the junction potential. Accuracy and precision were better than 0.002 pH units.

Solid Identification. Room-temperature transmission ^{57}-Fe−Mössbauer spectroscopy was used. ^{57}Fe−Mössbauer spectroscopy (MBS) is more sensitive to minor phases than is X-ray diffraction (XRD) (*33*, *34*). MBS measures the splitting of nuclear energy levels of ^{57}Fe as determined by protons and neutrons and their interactions with chemical environments, and therefore, long-range crystalline arrays are less essential than for analysis by XRD. The technique detects characteristic signals for dried HFO (ferrihydrite), which shows two or six disperse peaks with XRD. The sample density on the holder for MBS was 5 mg Fe/cm^2. Transmission electron microscopy (TEM, Phillips 420, Material Characterization Laboratory, The Pennsylvania State University) was used to measure particle size and shape. Copper mesh grids with an organic coating were briefly immersed into the diluted aliquots of suspensions and dried in a desiccator at room temperature before being transferred into the vacuum chamber of the TEM instrument. XRD patterns were recorded using Cu− Kα radiation with a 2°/min scanning rate (Scintag Pad V, Material Characterization Laboratory, The Pennsylvania State University) and analyzed using the Powder Diffraction Files (*35*). For MBS and XRD, samples were air-dried at 40 °C, thus retaining all water contributing to the heat of immersion (*36*).

Preparation of Hematite and Aging without Dilution. Thermal hydrolysis (refs *9* and *37* as modified in ref *38*) was used for the production of hematite. Twenty mM $FeCl_3$ was added to 2 mM HCl at 100 °C. The mixture was kept at 100 °C for 5 days with the frequent addition of pre-heated DI water to maintain the initial volume and synthesis temperature (100 °C). As soon as $FeCl_3$ was added, the suspension turned dark brown. The color became less intense after 3−4 h, and the solution turned orange−red within 1 day, indicating the formation of hematite.

After 5 days at 100 °C, the suspension was aged at room temperature for up to 193 days. MBS and TEM analyses of particles harvested on day 1 at room temperature confirmed the formation of spherical hematite particles 102 (±10) nm in diameter (average and standard deviation of 35 particles, synthetic hematite hereafter; Figure 1a,b). $[Fe(III)_{diss}]$ and pH were measured as a function of time. $[Fe(III)_{diss}]$ was typically determined as the Fe(III) concentration in the filtrate (0.1 μm), but similar results were obtained after centrifugation at 12 100*g* for 10 min. The TEM image indicated the aggregation of particles, which may explain why 0.1 μm filtration was as effective as centrifugation.

Commercial hematite (Fisher, reagent grade, >2 μm in diameter) was used as purchased. MBS and XRD confirmed its phase-purity (Figure 1c,d). The hematite was hydrated under the same concentrations of components: 20 mM Fe(III) dispersed in 62 mM HCl (final concentrations) at room temperature. The filterable $[Fe(III)_{diss}]$ and pH were measured as a function of time for up to 197 days.

Dilution of Fe^{3+} and H^+ after Sequential Centrifugation Followed by Additional Aging. On day 34, aliquots from the synthetic hematite suspension were sequentially centrifuged, decanted, and resuspended in deionized water, resulting in an increased pH due to dilution (i.e., with each sequential centrifugation, a known volume of supernatant was removed for analyses, and an identical volume of deionized water was added). At each sequential centrifugation step, one centrifuge tube that had a higher pH than the previous step was excluded from further centrifugation. The $[Fe(III)_{diss}]$ and pH values of the tubes were measured for up to an additional 163 days.

Dilution of Fe^{3+} and H^+ by Ultrafiltration. An identical synthetic hematite suspension was prepared and slowly filtered (with recirculation) through a 10 kDa membrane, with frequent additions of deionized water to maintain the initial volume. This was to increase the pH continually due to dilution with a short duration at each pH. The $[Fe(III)_{diss}]$ and pH values were measured in the permeates. The pH increased to ~5 during 3 days.

Results and Discussion

Aging without Dilution. The $[Fe(III)_{diss}]$ was 0.13 mM, and the pH was 1.20 after 1 day for synthetic hematite, indicating

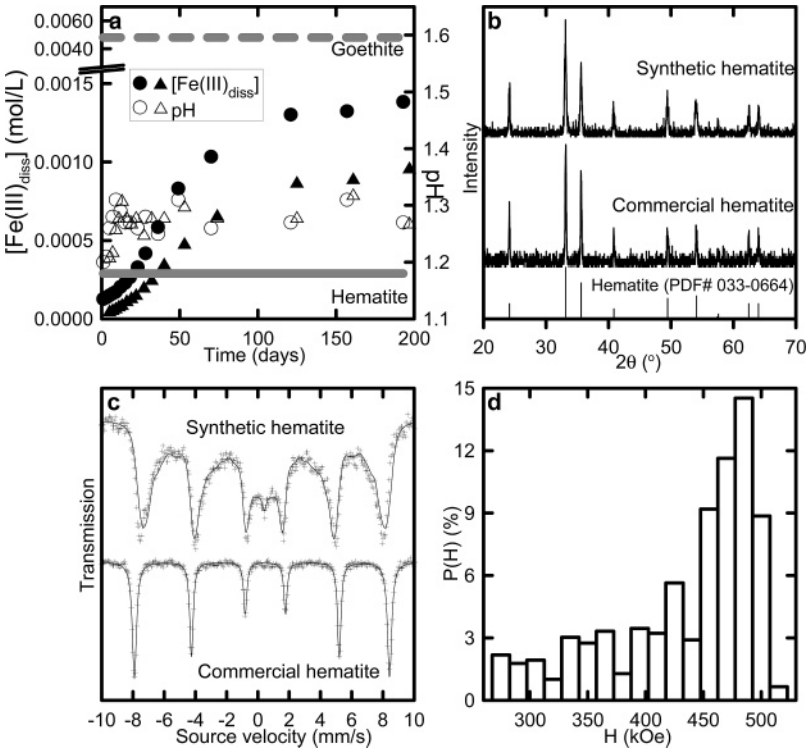

FIGURE 2. (a) Change in $[Fe(III)_{diss}]$ and pH vs time. Circles for synthetic hematite and triangles for commercial hematite. Gray lines represent solubilities of hematite and goethite predicted by NIST values at the final pH 1.29 (±0.02) (0.29 ± 0.04 and 4.8 ± 0.4 mM as $[Fe(III)_{diss}]$, respectively). (b) XRD of synthetic and commercial hematite at the end of experiments. The peak positions of reference hematite were also illustrated for comparison (PDF# 033-0664). No structural change was detected for both hematites. (c) MBS for synthetic and commercial hematite. Synthetic hematite deviates from ideal hematite (cf. Figure 1a), indicating that the extensive hydration of interfacial Fe^{3+} occurred without changing the hematite structure (refer to XRD in panel b). This behavior was not observed for commercial hematite due to a smaller ratio of surface/bulk Fe atom. (d) Distribution of magnetic hyperfine fields (H) determined from the MBS of the synthetic hematite (upper MBS in panel c).

transient undersaturation with respect to bulk hematite. The $[Fe(III)_{diss}]$ and pH increased with time. At 193 days, the $[Fe(III)_{diss}]$ was 1.4 mM, and the pH was 1.27, approaching the solubility of goethite (Figure 2a, solid and open circles for $[Fe(III)_{diss}]$ and pH). Hydration of the commercial hematite for the same chemical concentrations produced similar results (Figure 2a, solid and open triangles for $[Fe(III)_{diss}]$ and pH). The $[Fe(III)_{diss}]$ and pH values of the commercial hematite suspension at day 1 were 0.055 mM and 1.21, respectively. After 197 days, the $[Fe(III)_{diss}]$ and pH values were 0.97 mM and 1.27, respectively, well above the predicted solubility of hematite. XRD confirmed that both synthetic and commercial solids were invariably hematite after aging for 193 and 197 days, respectively (Figure 2b) (i.e., no structural changes occurred in the bulk phase).

Asymmetric peak broadening was observed after 193 days of aging the synthetic hematite under MBS (Figure 1a vs upper spectrum in Figure 2c), while the commercial hematite (>2 μm in diameter) showed characteristic peaks for bulk hematite even after 197 days of aging (lower spectrum in Figure 2c). No super-paramagnetic behavior was observed for the synthetic hematite, indicating that the particle size was larger than 41 nm (*38*, *39*). Broadening is due to the distribution of magnetic hyperfine fields within the particle (*40*, *41*). The upper spectrum in Figure 2c was analyzed using the Voigt-based fitting (VBF) procedure (*42*, *43*) to determine the distribution of magnetic hyperfine fields. The master class of magnetic hyperfine fields (**H**) of the synthetic hematite was located at 480 kOe (Figure 2d). The values for magnetic hyperfine field for hematite of comparable sizes range from 506 to 515 kOe (*44*). The master class of the hyperfine field is located at 340−360 kOe for goethite (*45*, *46*).

Asymmetric peak broadening has been attributed to a high proportion of interfacial Fe^{3+} with relaxed magnetic hyperfine fields (*40*, *41*). The relaxation of magnetic hyperfine fields from >506 to 480 kOe means that the interstitial ligand (O^{2-}) around Fe^{3+} was replaced by OH^- and H_2O due to hydration, which resulted in the dissolution of Fe(III) from the hydrated interface (Figure 2a). The increase of $[Fe(III)_{diss}]$ cannot be attributed to the dissolution of preformed more soluble phases since both initial hematites were free from impurity (Figure 1) and the suspension was never supersaturated for any other soluble phase (Figure 2a).

The magnetic hyperfine field (**H**) is a measure of nuclear energy level splitting caused by the interaction between an effective magnetic hyperfine field on the Fe nucleus posed by lattice ligands and the magnetic moment of the nucleus (*43*). In other words, the value of **H** is a function of the identity and arrangement of ligands that pose the effective magnetic hyperfine field around Fe^{3+}. Chemisorption of polar molecules (e.g., ammonia, H_2O, CO, etc.) changes the chemical environments of interfacial Fe atoms (*47*). Therefore, the distribution of magnetic hyperfine fields indicates that there is a distribution of chemical environments for Fe nuclei within the structure of synthetic hematite (~100 nm) due to hydration (Figure 3). Those layers were not detected in the commercial hematite due to the decreased proportion of interfacial Fe with larger particles. Similarly, the calorimetric measurement of heat capacity upon which the free energy of formation for bulk hematite is based would not account for interfacial layers since the calorimetry for heat capacity involves thermal equilibration throughout the entire particle in the absence of water (*30*).

Dilution Experiments. Sequential centrifugation was performed to observe the change of $\{Fe^{3+}\}$ and pH upon dilution by DI water (Figure 4a,b). The samples were aliquots taken from a 34 day aged synthetic hematite suspension, where we observed the continuous increase of $[Fe(III)_{diss}]$

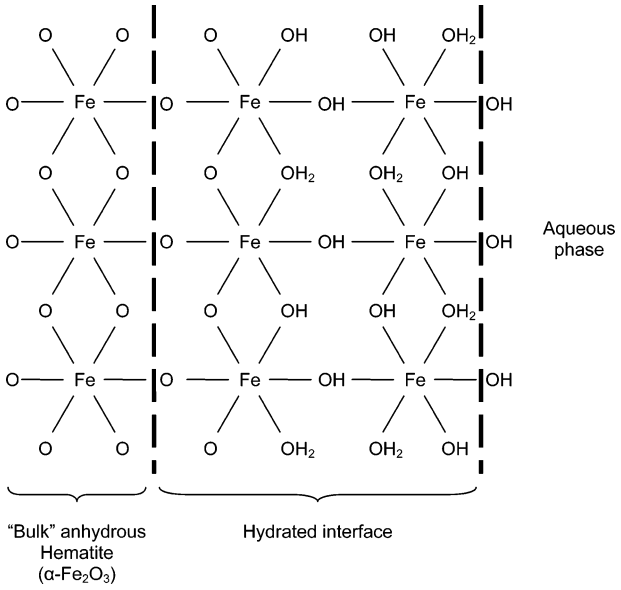

FIGURE 3. Model for interface between water and hematite (modified from refs *14* and *15*), showing penetration of water through several layers. Estimated thickness of the layers ranges from 2.6 to 3.4 nm (*14*–*16*).

(Figure 2a). The $[Fe(III)_{diss}]$ and pH values from the aliquots were measured during an additional 163 days of aging; $\{Fe^{3+}\}$ values were computed using visual MINTEQ and equilibrium constants in Table 1 (Figure 4a). The $\{Fe^{3+}\}$ and pH values predicted by dilution are designated as × in Figure 4a. All of the sample sets were supersaturated with respect to hematite. Sample sets 1 and 2 were initially undersaturated, while sample sets 3, 4, and 5 were initially supersaturated with respect to goethite. Although all samples were in supersaturation with hematite throughout the experiment, the $\{Fe^{3+}\}$ values did not approach the hematite solubility predicted by thermodynamic properties of bulk hematite and were consistent with the solubility of goethite for 163 days. However, XRD indicated that the solids were invariably hematite (Figure 4b), indicating that the bulk phase is hematite.

In another dilution experiment using ultrafiltration where the pH was increased continually with a short duration at each pH value (less than 2 h), $\{Fe^{3+}\}$ increased faster (Figure 4c). The total duration of the ultrafiltration was 3 days. This is consistent with the hydration of hematite without dilution, resulting in higher $[Fe(III)_{diss}]$ and pH values (Figure 2a). As dilution continued and the pH rose above 2.0, $\{Fe^{3+}\}$ decreased and approached the solubility of HFO. Further dilution to pH >3.2 resulted in $\{Fe^{3+}\}$ and pH values similar to those for goethite. Precipitation of HFO is unlikely since $\{Fe^{3+}\}$ increased from undersaturation with HFO. Plus, MBS identified the solid collected at the end of the procedure as hematite (Figure 4d). Although we used ~100 nm synthetic hematite for this procedure as well, asymmetric peak broadening due to the distribution of hyperfine magnetic fields did not develop (Figure 4d vs upper MBS in Figure 2c). This indicates that, although the mechanism is unclear from this study, the faster continual pH increase developed hydrated layers that are thinner but more soluble. Samson et al. (*48*, *49*) showed that the dissolution rate of hematite

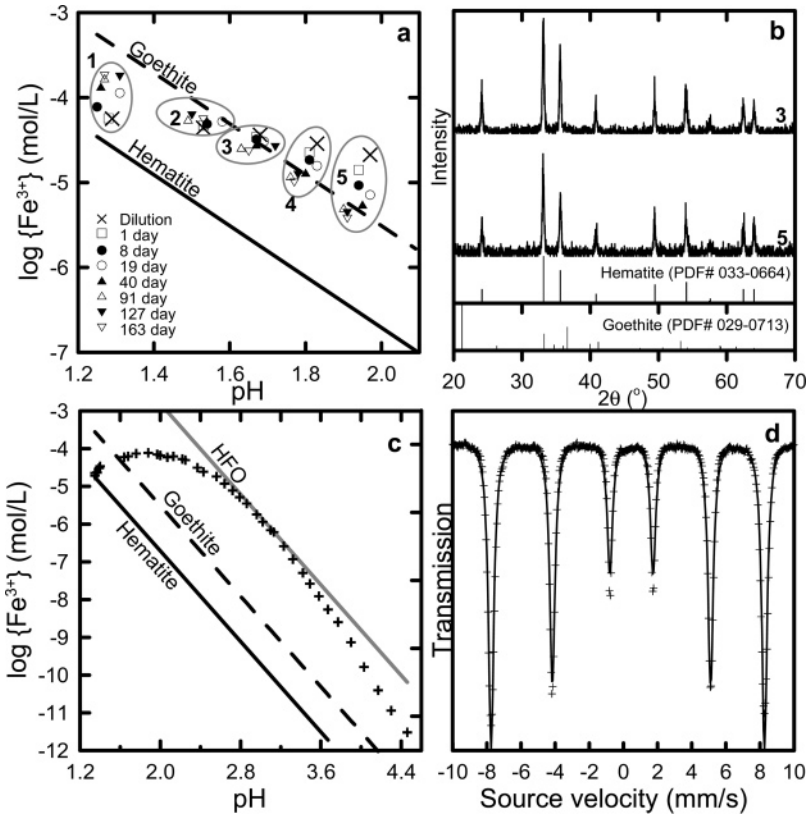

FIGURE 4. (a) Time-dependent changes in activities of Fe^{3+} ($\{Fe^{3+}\}$) and pH of centrifuged samples. Numbers identify each centrifuge tube of different pH values, from which $[Fe(III)_{diss}]$ and pH in the corresponding gray ovals were measured as a function of time. Tube 1 represents the aged sample without dilution. Days in legends represent the additional aging time after 34 days of aging of the initial suspension. For all conditions, solubility was consistent with goethite. (b) XRD of tubes 3 and 5, which once experienced equilibrium and supersaturation with respect to goethite, respectively, after 163 days of aging. Both patterns confirmed that the solids were hematite, not goethite. XRD and MBS for tube 1 (undersaturation with respect to goethite) are illustrated in Figure 2b,c. (c) Changes of $\{Fe^{3+}\}$ and pH in permeates from ultrafiltration. (d) MBS for hematite particles harvested at the end of the ultrafiltration (3 days).

TABLE 1. Hydrolysis Constants for Fe^{3+} and Solubility Products for Hematite, Goethite, and Ferrihydrite (*4*)

aqueous species	log $*\beta^a$
$FeOH^{2+}$	−2.19
$Fe(OH)_2^{1+}$	−4.59
$Fe(OH)_4^-$	−21.59
$Fe_2(OH)_2^{4+}$	−2.85
$Fe_3(OH)_4^{5+}$	−6.29
solid phases	**log $*K_{sp}^b$**
α-Fe_2O_3 (hematite)	−0.71
α-FeOOH (goethite)	0.49
ferrihydrite	3.19

[a] Stability constants ($*\beta$) are defined for reactions: $mFe^{3+} + nH_2O \leftrightarrow Fe_m(OH)_n^{(3m-n)+} + nH^+$. [b] $*K_{sp} = \{Fe^{3+}\}/\{H^+\}^3$.

increased significantly when the hematite was hydrated prior to dissolution, especially when the hematite was hydrated at higher pH values. They attributed this to faster ligand-exchange of surface bound Fe^{3+} at neutral pH, analogous to the faster water-exchange for $Fe(OH)^{+2}$ as compared to Fe^{3+}.

Implications for Environmental Fe Chemistry. Our results indicate that the hydration of hematite has been underestimated in dealing with aqueous reactions that involve hematite. XRD indicated insignificant structural modification of hematite (Figures 2b and 4b), while MBS documented the development of distribution of hyperfine magnetic fields within the hematite (Figure 1a vs Figure 2c). These observations suggest that the interstitial O^{2-} in several layers of hematite was replaced with OH^- and H_2O due to hydration (*50*) (Figure 3), and as a result, $\{Fe^{3+}\}$ increased from the thermodynamic solubility of hematite and became more consistent with goethite or HFO, which are hydrated soluble analogues for hematite (Figures 2a and 4a,c). The observed increase of solubility was more than could be explained by the modified Ostwald−Freundlich equation, accounting for surface free energy (*51*, *52*).

These results have important implications in assessing abiotic and microbial redox reactions since the potential for the Fe(III)/Fe(II) couple is proportional to $\log\{Fe^{3+}\}$. This could result in an order of magnitude change in the predicted ratio of contaminant concentrations (reduced/oxidized) for a one-electron transfer and a two-log unit decrease for a two-electron transfer reaction.

Our results help to explain anomalously higher-than-expected electrochemical potentials measured in a ferrous iron/hematite system (*2*, *19*), requirement of a higher solubility product of hematite for thermodynamic interpretation of weathering profiles (*53*), and time-dependent increase of surface protonation (*14*, *15*). Results from the instrumental analysis of the hydrated surface of hematite (*21*, *22*) are also consistent with our observation that the hydration of hematite results in interfacial layers with thermodynamic characteristics of goethite rather than of bulk hematite.

Acknowledgments

This research was supported by the Office of Science (BER), U.S. Department of Energy, Grant DE-FG02-01-04ER63914 and by the National Science Foundation under Grant BES-0523196.

Literature Cited

(1) Stumm, W.; Sulzberger, B. The cycling of iron in natural environments: Considerations based on laboratory studies of heterogeneous redox processes. *Geochim. Cosmochim. Acta* **1992**, *56*, 3233−3257.

(2) Grenthe, I.; Stumm, W.; Laaksuharju, M.; Nilsson, A.-C.; Wikberg, P. Redox potentials and redox reactions in deep groundwater systems. *Chem. Geol.* **1992**, *98*, 131−150.

(3) Charlet, L.; Silvester, E.; Liger, E. N-Compound reduction and actinide immobilization in surficial fluids by Fe(II): The surface $\equiv Fe^{III}OFe^{II}OH^0$ species, as major reductant. *Chem. Geol.* **1998**, *151*, 85−93.

(4) NIST. *NIST Critically Selected Stability Constants of Metal Complexes Database*; U.S. Department of Commerce: Washington, DC, 2004.

(5) Smith, R. M.; Martell, A. E. *Critical Stability Constants, Vol. 4: Inorganic Complexes*; Plenum: New York, 1976.

(6) Chase, M. W., Jr. NIST-JANAF Thermochemical Tables, Parts I and II. *J. Phys. Chem. Ref. Data* **1998**, *9*.

(7) Robie, R. A.; Hemingway, B. S. Thermodynamic properties of minerals and related substances at 298.15 K and 1 bar (10^5 Pa) pressure and at higher temperatures; U.S. Geological Survey Bulletin 2131; USGS: Washington, DC, 1995; 461 pp.

(8) Parks, G. S.; Kelley, K. K. The heat capacities of some metallic oxides. *J. Phys. Chem.* **1926**, *30*, 47−55.

(9) Cornell, R. M.; Schwertmann, U. *The Iron Oxides: Structure, Properties, Reactions, Occurrence, and Uses*; VCH Publisher: New York, 1996.

(10) Ferrier, A. Influence de l'etat de division de la goethite et de l'oxyde ferrique sur leurs chaleurs de reaction. *Rev. Chim. Miner.* **1966**, *3*, 587−615.

(11) King, E. G.; Weller, W. W. Low-temperature heat capacities and entropies at 298.15 K of goethite and pyrophyllite. *U.S. Bur. Mines, Rep. Invest.* **1970**, *7369*, 6.

(12) Langmuir, D. Particle size effect on the reaction goethite = hematite + water. *Am. J. Sci.* **1971**, *271*, 147−156.

(13) Langmuir, D. Correction: Particle size effect on the reaction goethite = hematite + water. *Am. J. Sci.* **1972**, *272*, 972.

(14) Onoda, G. Y., Jr.; de Bruyn, P. L. Proton adsorption at the ferric oxide/aqueous solution interface. I. A kinetic study of adsorption. *Surf. Sci.* **1966**, *4*, 48−63.

(15) Berube, Y. G.; Onoda, G. Y., Jr.; de Bruyn, P. L. Proton adsorption at the ferric oxide/aqueous solution interface. II. Analysis of kinetic data. *Surf. Sci.* **1967**, *8*, 448−461.

(16) Dumont, F.; Watillon, A. Stability of ferric oxide hydrosols. *Discuss. Faraday Soc.* **1971**, *52*, 352−360.

(17) Zettlemoyer, A. C.; McCafferty, E. The heat of immersion on α-Fe_2O_3 in water. *Z. Phys. Chem. Neue Folge* **1969**, *64*, 41−48.

(18) McCafferty, E.; Zettlemoyer, A. C. Adsorption of water vapor on α-Fe_2O_3. *Discuss. Faraday Soc.* **1971**, *52*, 239−254.

(19) Macalady, D. L.; Langmuir, D.; Grundl, T.; Elzerman, A. Use of model-generated Fe^{3+} ion activities to compute E_h and ferric oxyhydroxide solubilities in anaerobic systems. In *Chemical Modeling of Aqueous Systems II*; Melchior, D. C., Bassett, R. L., Eds.; American Chemical Society: Washington, DC, 1990; Vol. 416, pp 350−367.

(20) Silvester, E.; Charlet, L.; Tournassat, C.; Gehin, A.; Greneche, J.-M.; Liger, E. Redox potential measurements and Mössbauer spectrometry of Fe^{II} adsorbed onto Fe^{III} (oxyhydr)oxides. *Geochim. Cosmochim. Acta* **2005**, *69*, 4801−4815.

(21) Eggleston, C. M.; Stack, A. G.; Rosso, K. M.; Bice, A. M. Adatom Fe(III) on the hematite surface: Observation of a key reactive surface species. *Geochem. Trans.* **2004**, *5*, 33−40.

(22) Trainor, T. P.; Chaka, A. M.; Eng, P. J.; Newville, M.; Waychunas, G. A.; Catalano, J. G.; Brown, J. G. E. Structure and reactivity of the hydrated hematite (0001) surface. *Surf. Sci.* **2004**, *573*, 204−224.

(23) Liu, P.; Kendelewicz, T.; Brown, G. E.; Nelson, E. J.; Chambers, S. A. Jr. Reaction of water vapor with α-Al_2O_3(0001) and α-Fe_2O_3-(0001) surfaces: Synchrotron X-ray photoemission studies and thermodynamic calculations. *Surf. Sci.* **1998**, *417*, 53−65.

(24) Junta-Rosso, J. L.; Hochella, M. F. The chemistry of hematite (001) surfaces. *Geochim. Cosmochim. Acta* **1996**, *60*, 305−314.

(25) Catalano, J. G.; Zhang, Z.; Fenter, P.; Bedzyk, M. J. Inner-sphere adsorption geometry of Se(IV) at the hematite (100)−water interface. *J. Colloid Interface Sci.* **2006**, *297*, 665−671.

(26) Catalano, J. G.; Zhang, Z.; Park, C.; Fenter, P.; Bedzyk, M. J. Bridging arsenate surface complexes on the hematite (012) surface. *Geochim. Cosmochim. Acta* **2007**, *71*, 1883−1897.

(27) Gronvold, F.; Westrum, E. F., Jr. α-Ferric oxide: Low temperature heat capacity and thermodynamic functions. *J. Am. Chem. Soc.* **1959**, *81*, 1780−1783.

(28) Gronvold, F.; Samuelsen, E. J. Heat capacity and thermodynamic properties of α-Fe_2O_3 in the region of 300−1050 K antiferromagnetic transition. *J. Phys. Chem. Solids* **1975**, *36*, 249−256.

(29) Nordstrom, D. K.; Munoz, J. L. *Geochemical Thermodynamics*; The Benjamin/Cummings Publishing Company, Inc.: San Francisco, 1985.
(30) Robie, R. A.; Hemingway, B. S. Calorimeters for heat of solution and low-temperature heat capacity measurements. *U.S. Geol. Survey Prof. Paper* **1972**, *755*, 32.
(31) APHA. *Standard Methods for the Examination of Water and Wastewater*, 18th ed.; American Public Health Association: Washington, DC, 1992.
(32) Viollier, E.; Inglett, P. W.; Hunter, K.; Roychoudhury, A. N.; Van Cappellen, P. The ferrozine method revisited: Fe(II)/Fe(III) determination in natural waters. *Appl. Geochem.* **2000**, *15*, 785−790.
(33) Murad, E. Application of ^{57}Fe Mössbauer spectroscopy to problems in clay mineralogy and soil science: Possibilities and limitations. *Adv. Soil Sci.* **1990**, *12*, 125−157.
(34) Hawthorne, F. C. Mössbauer spectroscopy. In *Spectroscopic Methods in Mineralogy and Geochemistry*; Hawthorne, F. C., Ed.; Mineralogical Society of America: Washington, DC, 1988; Vol. 18.
(35) JCPDS Powder Diffraction File. *Organic and Organometallic Phases Search Manual. Hanawalt Index, Alphabetical Index, and Organic Formula Index*; 1994.
(36) Zettlemoyer, A. C.; McCafferty, E. Water on oxide surfaces. *Croat. Chem. Acta* **1973**, *45*, 173−187.
(37) Matijevic, E.; Scheiner, P. Ferric hydrous oxide sols. III. Preparation of uniform particles by hydrolysis of Fe(III)-chloride, -nitrate, and -perchlorate solutions. *J. Colloid Interface Sci.* **1978**, *63*, 509−524.
(38) Raming, T. P.; Winnubst, A. J. A.; van Kats, C. M.; Philipse, A. P. The synthesis and magnetic properties of nanosized hematite (α-Fe_2O_3) particles. *J. Colloid Interface Sci.* **2002**, *249*, 346−350.
(39) Kündig, W.; Bömmel, H.; Constabaris, G.; Lindquist, R. H. Some properties of supported small α-Fe_2O_3 particles determined with the Mössbauer effect. *Phys. Rev.* **1966**, *142*, 327−333.
(40) van der Kraan, A. M. Mössbauer effect studies of surface ions of ultrafine α-Fe_2O_3 particles. *Phys. Status Solidi A* **1973**, *18*, 215−226.
(41) Shinjo, T.; Kiyama, M.; Sugita, N.; Watanabe, K.; Takada, T. Surface magnetism of α-Fe_2O_3 by Mössbauer spectroscopy. *J. Magn. Magn. Mater.* **1983**, *35*, 133−135.
(42) Rancourt, D. G.; Ping, J. Y. Voigt-based methods for arbitrary-shape static hyperfine parameter distributions in Mössbauer spectroscopy. *Nucl. Instrum. Methods Phys. Res., Sect. B* **1991**, *58*, 85−97.
(43) Lagarec, K.; Rancourt, D. G. *Recoil: Mössbauer Spectral Analysis Software for Windows, version 1.0*; 1998.
(44) Hobson, M. C. J.; Gager, H. M. A. Mössbauer effect study on crystallites of supported ferric oxide. *J. Catal.* **1970**, *16*, 254−263.
(45) Murad, E. The characterization of goethite by Mössbauer spectroscopy. *Am. Mineral.* **1982**, *67*, 1007−1011.
(46) Jang, J.-H.; Dempsey, B. A.; Catchen, G. L.; Burgos, W. D. Effects of Zn(II), Cu(II), Mn(II), Fe(II), NO_3^-, or SO_4^{2-} at pH 6.5 and 8.5 on transformations of hydrous ferric oxide (HFO) as evidenced by Mössbauer spectroscopy. *Colloids Surf., A* **2003**, *221*, 55−68.
(47) Hobson, M. C., Jr. Surface studies by Mössbauer spectroscopy. *Adv. Colloid Interface Sci.* **1971**, *3*, 1−43.
(48) Samson, S. D.; Eggleston, C. M. The depletion and regeneration of dissolution-active sites at the mineral−water interface: II. Regeneration of active sites on α-Fe_2O_3 at pH 3 and 6. *Geochim. Cosmochim. Acta* **2000**, *64*, 3675−3683.
(49) Samson, S. D.; Stillings, L. L.; Eggleston, C. M. The depletion and regeneration of dissolution-active sites at the mineral−water interface: I. Fe, Al, and In sesquioxides. *Geochim. Cosmochim. Acta* **2000**, *64*, 3471−3484.
(50) Wolska, E.; Szajda, W. Structural and spectroscopic characteristics of synthetic hydrohematite. *J. Mater. Sci.* **1985**, *20*, 4407−4412.
(51) Corey, R. B. Adsorption versus precipitation. In *Adsorption of Inorganics at Solid−Liquid Interfaces*; Anderson, M. A., Rubin, A. J., Eds.; Ann Arbor Science: Ann Arbor, MI, 1981; pp 161−182.
(52) Langmuir, D. The Gibbs free energies of substances in the system Fe-O_2-H_2O-CO_2 at 25 °C. *U.S. Geol. Survey Prof. Paper* **1969**, *650*, 180−184.
(53) Tardy, Y.; Nahon, D. Geochemistry of laterites and stability of Al-goethite, Al-hematite, and Fe^{3+}-kaolinite in bauxites and ferricretes: An approach to the mechanism of concretion formation. *Am. J. Sci.* **1985**, *285*, 865−903.

Received for review March 2, 2007. Revised manuscript received August 4, 2007. Accepted August 18, 2007.

ES070535T